metals

MDPI

Article

Research on Reduced-Order Model of Heat Treatment Online Simulation for Digital Twin Application

Miao Gong [1,2], Daming Tong [1,2,*], Xingyun Yang [1,2], Chuanwei Li [1,2] and Jianfeng Gu [1,2]

[1] Shanghai Key Laboratory of Materials Laser Processing and Modification, School of Materials Science and Engineering, Shanghai Jiao Tong University, Shanghai 200240, China; gongmiao@sjtu.edu.cn (M.G.); 16340824150548@sjtu.edu.cn (X.Y.); li-chuanwei@sjtu.edu.cn (C.L.); gujf@sjtu.edu.cn (J.G.)
[2] Institute of Materials Modification and Modelling, School of Materials Science and Engineering, Shanghai Jiao Tong University, Shanghai 200240, China
* Correspondence: daming_tong@sjtu.edu.cn

Abstract

Digital twin technology puts forward higher requirements on the real-time performance of simulations. In order to realize the online simulation of the heat treatment process, a transient temperature field-microstructure field coupling calculation method based on the reduced-order model was constructed. This mathematical model was applied to the online simulation of the end-quenching treatment of 42CrMo steel with complex time-varying water spray. The results show that the utilization of a 10th-order reduced-order model diminishes the total computation time from 1 h to 3.4 s, with a reduction in storage requirements by a factor of 610. The calculation accuracy of the reduced-order model is 99.2%, which satisfies the requirements of real-time online simulation. A framework for the heat treatment digital twin system has been proposed and an online simulation platform for end-quenching treatment was developed. The single-step calculation time for the proposed platform is 0.4 s. The online simulation temperature is basically consistent with the measured temperature results. This work provides novel avenues for fast calculation and real-time control of the heat treatment process.

Keywords: heat treatment; digital twin; reduced-order model; end-quenching; intelligent heat treatment

1. Introduction

With the continuous advancement of machine learning, artificial intelligence and related technologies, intelligent heat treatment has become one of the core innovative technologies of heat treatment, and there is also a strong demand for the transformation and upgrading of heat treatment technology. It is difficult to implement process regulation in the heat treatment process by using the traditional monitoring-feedback-control method, which restricts the development of intelligent heat treatment. The fundamental challenge lies in achieving real-time monitoring of the heat treatment process. Digital twins, serving as digital representations of tangible objects, have progressively evolved into a significant technological instrument for intelligence, enabling comprehensive real-time monitoring and control of physical entities from all perspectives [1,2]. The digital twin necessitates the spatial description of both the intrinsic and extrinsic behaviors of the actual physical entity. Additionally, it demands online and real-time capabilities [3], which consequently impose an elevated requirement for computational speed [4].

Check for updates

Academic Editor: Noé Cheung

Received: 21 January 2026
Revised: 11 February 2026
Accepted: 26 February 2026
Published: 28 February 2026

Copyright: © 2026 by the authors. Licensee MDPI, Basel, Switzerland. This article is an open access article distributed under the terms and conditions of the Creative Commons Attribution (CC BY) license.

Multi-physics coupling numerical simulation is one of the important methods for carrying out heat treatment research, which can reflect the internal behaviors of temperature, phase transformation, stress, deformation and other aspects of the part during heat treatment [5]. Currently, the principal numerical simulation methods employed for heat treatment include finite element, finite difference, and finite volume methods. Nonetheless, due to the substantial degrees of freedom inherent in the model, the numerical simulation entails solving a substantial number of partial differential equations at each increment step during iteration processes [6]. Even with the utilization of a high-performance computer, the computational time extends to several hours or even days, making it challenging to fulfill the real-time simulation requirements demanded by digital twin technology [7].

The reduced-order model (ROM) technology involves employing a condensed model to capture the essential features of the original full-order model (FOM). This approach reduces the complexity of partial differential equations within finite element computations and enhances computational efficiency. The Proper Orthogonal Decomposition (POD) method [8] is a predominant model reduction technique that has been extensively applied in various research fields, including fluid dynamics systems [9,10], mechanical systems [11,12] and electrical power systems [13]. Ansari [14] employed the POD method to simulate the electrochemical behavior of the proton exchange membrane fuel cell, including the porosity of catalyst layers, cell temperature, and concentration of inlet oxygen. Compared to the traditional finite volume method, the POD method improves the computational efficiency by dozens of times. Some researchers have utilized the POD method to establish static response models, aiming to enhance computational speed. For instance, both Chen [15] and Aversano [16] assembled a snapshot matrix based on the fluid dynamics calculation results under different boundary conditions. Specifically, Chen [15] constructed the snapshot matrix from 585 simulations under different combinations of boiler operating conditions, including variations in fuel distribution and air flow parameters. Aversano [16] generated 64 samples by varying inlet velocity and inlet CH_4 molar fraction to assemble the snapshot matrix. After applying POD reduction to these matrices, they employed surrogate models [17] such as Kriging or support vector machines to establish the relationship between input and output, facilitating rapid simulation computations of the system with respect to input parameters. However, this type of static response method is not suitable for intricate transient physical processes, such as a heat treatment process. Wang [18] proposed a finite element reduction model for the transient fluid–solid coupling temperature field calculation of oil-immersed transformers. This model led to a reduction in calculation time from hours to seconds, which is suitable for building digital twin models. Li [19] proposed a POD-ROM model for the calculation of fluid flow and heat transfer process in a fractured geothermal reservoir. The computational efficiency can be improved by 10–15 times and the maximum prediction error is 0.83%. Some researchers have also demonstrated the suitability of ROM in transient physical field calculations involving nonlinear parameters [20] and complex time-varying boundary conditions [21]. However, it remains unclear whether ROMs built from snapshots under a single boundary condition can accurately predict responses under the strongly time-varying conditions typical of heat treatment. In addition, the coupling between temperature evolution and phase transformation may further reduce computational efficiency, challenging the use of these models for real-time digital twin simulations in heat treatment.

The online simulation of the heat treatment process demands swift solutions for transient physical fields throughout the entire procedure. Employing conventional approaches, such as reducing the number of mesh or improving hardware performance, proves challenging in achieving real-time online simulation. Particularly in intricate heat treatment processes such as water-air alternating quenching [22], the real-time computa-

tion of temperature-microstructure fields becomes even more challenging. In this study, the POD method is employed to establish a transient temperature-microstructure fields ROM for intricate end-quenching processes. For the transient state process, the FOM must solve 5268 partial differential equations simultaneously, whereas the ROM needs to solve 10 equations. The computational efficiency of the proposed model improved by 1062 times while a maximum calculation error of 0.8% is maintained. This work offers novel insights for real-time control and rapid computation in the context of the heat treatment process.

2. Numerical Model

2.1. Full-Order Model of the Temperature Field Computation

The efficiency and accuracy of the temperature field computation significantly influence the efficiency and precision of microstructures and other physical field calculations. The governing equation commonly employed for FOM of temperature field computation is the Fourier heat conduction equation, as described below:

$$k\nabla^2 T + Q - \rho c_p \frac{\partial T}{\partial t} = 0 \tag{1}$$

where T is temperature; k, c_p, ρ are thermal conductivity, specific heat and density, respectively; t is time; Q is the heat source, which is a latent heat of phase transformation during heat treatment. In this study, the material is assumed to be isotropic, and the thermal properties are considered temperature-dependent to account for nonlinearity. Due to the small magnitude of deformations during heat treatment, the heat generated by plastic strains is negligible. Utilizing Galerkin's weighted residual method, and employing shape functions as weighting functions for the temperature field governing equation and boundary conditions, the finite element solution equation for the temperature field can be derived as follows [23]:

$$\boldsymbol{K}\boldsymbol{T} + \boldsymbol{M}\dot{\boldsymbol{T}} = \boldsymbol{F} \tag{2}$$

$$\boldsymbol{K} = \int_{\Omega} k\boldsymbol{B}^T\boldsymbol{B}d\Omega + \int_{\Gamma_3} h\boldsymbol{N}^T\boldsymbol{N}d\Gamma \tag{3}$$

$$\boldsymbol{M} = \int_{\Omega} \rho c_p \boldsymbol{N}^T\boldsymbol{N}d\Omega \tag{4}$$

$$\boldsymbol{F} = \int_{\Omega} \boldsymbol{N}^{\mathrm{T}} Q d\Omega + \int_{\Gamma_3} h\boldsymbol{N}^{\mathrm{T}} T_f d\Gamma \tag{5}$$

where $\boldsymbol{T}$ is nodal temperature column vector; $\dot{\boldsymbol{T}}$ is temporal derivative of $\boldsymbol{T}$; $\boldsymbol{K}$, $\boldsymbol{M}$ and $\boldsymbol{F}$ are stiffness matrix, mass matrix and load vector, respectively; h is heat transfer coefficient $\boldsymbol{N}$ is element shape function matrix; Ω is integration domain; Γ is the boundary of Ω, $\boldsymbol{B}$ is gradient of the shape function matrix.

The evolution of the temperature field can be divided into discrete time steps during transient calculation. Based on the temperature field at the ith time step and the time step increment, the temperature field at the $(i+1)$th time step can be computed. Therefore, the evolution of the field variable at different time instants can be sequentially calculated by giving the initial temperature field. The transient temperature field calculation equation can be obtained by using the backward difference method:

$$\left(\frac{\boldsymbol{M}}{\Delta t_{i+1}} + \boldsymbol{K}\right)\boldsymbol{T}_{i+1} = \boldsymbol{F} + \frac{\boldsymbol{M}}{\Delta t_{i+1}}\boldsymbol{T}_i \tag{6}$$

where Δt_{i+1} is the time step of $(i+1)$th. By employing the nodal temperature values at the nth step $\boldsymbol{T}_i$, the nodal temperature values at the $(i+1)$th step $\boldsymbol{T}_{i+1}$, can be obtained using the equation mentioned above.

Equation (6) represents the FOM of transient temperature field computation. From this equation, it is evident that matrices $\boldsymbol{K}$ and $\boldsymbol{M}$ are of size $n \times n$, where n is the total number of nodes. Consequently, solving a system of n-order linear equations is required in each time step. When dealing with a substantial number of elements, solving large-scale linear systems can be time-consuming, making it challenging to meet the real-time demands of online simulations. Therefore, it is necessary to reduce the computational complexity, thereby achieving the objective of rapid computation.

2.2. Reduced-Order Model of Temperature Field Computation

The main purpose of the transient temperature field ROM is to reduce the stiffness matrix, mass matrix, and load vector of the FOM (Equation (6)). The reduced model can retain the principal modes of the original matrix, thereby encapsulating the primary features of the FOM. Additionally, the reduced model diminishes the matrix dimensions, enabling efficient approximation solutions for the linear equation system. The present study employs the POD method for model reduction. This approach involves establishing an optimal set of orthogonal bases that can effectively represent the full-order system, using a snapshot matrix derived from computational results of the FOM. These orthogonal bases effectively capture the essence of the full-order system. Subsequently, model reduction is achieved by truncating the first s orthogonal basis vectors. Based on the Sirovich method [24], the snapshot matrix $\boldsymbol{A}$ can be constructed by nodal temperature values at m moments as follows:

$$\boldsymbol{A} = [\boldsymbol{T}_1, \boldsymbol{T}_2, \ldots \boldsymbol{T}_m] \tag{7}$$

where $\boldsymbol{T}_t$ represents the nodal temperature values at t time as follows:

$$\boldsymbol{T}_t = \left[\boldsymbol{T}_t^1, \boldsymbol{T}_t^2, \ldots, \boldsymbol{T}_t^n\right]^T \tag{8}$$

Performing Singular Value Decomposition (SVD) on matrix $\boldsymbol{A}$ results in:

$$\boldsymbol{A} = \boldsymbol{U}\boldsymbol{\Sigma}\boldsymbol{V}^T \tag{9}$$

where $\boldsymbol{U}$ and $\boldsymbol{V}$ are the left and right singular vector matrices, respectively, both of which are orthogonal matrices. $\boldsymbol{\Sigma}$ is a diagonal matrix where the singular values σ_i are arranged in decreasing order along the diagonal. The magnitudes of the singular values directly reflect the importance of the corresponding orthogonal vectors $\boldsymbol{U}$ and $\boldsymbol{V}$ in capturing the essential characteristics of the snapshot matrix $\boldsymbol{A}$.

By retaining the first s terms of $\boldsymbol{U}$, the POD orthogonal basis $\boldsymbol{P}_s$ can be obtained:

$$\boldsymbol{P}_s = \boldsymbol{U}_s = [u_1, u_2, \ldots, u_s] \tag{10}$$

The nodal temperature can be reconstructed by using the following equation:

$$\widetilde{\boldsymbol{T}}_t = \boldsymbol{P}\boldsymbol{\alpha}_t \tag{11}$$

where $\widetilde{\boldsymbol{T}}_t$ is the reconstructed nodal temperature at time t. $\boldsymbol{\alpha}_t$ is the coefficient column vector of the orthogonal basis at time t, which corresponds to the columns of $\boldsymbol{\Sigma}\boldsymbol{V}^T$ in the SVD of the snapshot matrix and is used, together with the retained POD modes, to reconstruct the nodal temperature at that time. The reconstruction accuracy can be evaluated using the energy proportion of the POD mode $\boldsymbol{I}_s$.

$$\boldsymbol{I}_s = \sum_{i=1}^{s} {\sigma_i}^2 / \sum_{i=1}^{m} {\sigma_i}^2 \tag{12}$$

Substituting Equation (11) into the FOM of the transient temperature field (Equation (6)) and multiplying both sides of the equation by $\boldsymbol{P_s}^T$, the ROM of the transient temperature field can be derived as follows:

$$\left(\boldsymbol{P_s}^{\mathrm{T}}\frac{\boldsymbol{M}}{\Delta t_{i+1}}\boldsymbol{P_s}+\boldsymbol{P_s}^{\mathrm{T}}\boldsymbol{K}\boldsymbol{P_s}\right)\boldsymbol{\alpha}_{i+1}=\boldsymbol{P_s}^{\mathrm{T}}\boldsymbol{F}+\boldsymbol{P_s}^{\mathrm{T}}\frac{\boldsymbol{M}}{\Delta t_{i+1}}\boldsymbol{P_s}\boldsymbol{\alpha}_i \tag{13}$$

From the equation, it can be observed that the temperature computation equation has transformed from calculating the temperature of all nodes to computing the coefficients $\boldsymbol{\alpha}$ of the orthogonal basis. The nodal temperature can be subsequently calculated by using Equation (11). As the dimension of $\boldsymbol{\alpha}$ is s, which is significantly smaller than the node number n, the solution time for the linear equation system of ROM is significantly reduced.

2.3. Microstructure Computation

Solid-state phase transformations in the heat treatment process can be categorized into diffusional and non-diffusional phase transformations based on the underlying mechanisms. The pearlite transformation and bainite transformation in steel are typically considered diffusional phase transformations, while the martensitic transformation is a non-diffusional phase transformation. For isothermal processes, the kinetics of diffusional phase transformations can be described using the Johnson–Mehl–Avrami–Kolmogorov (JMAK) equation:

$$f=1-\exp\left(-b\left(t-t_s\right)^n\right) \tag{14}$$

where f is the transformed fraction, t is time, and t_s is the incubation period. The parameters b and n are temperature-dependent and can be computed based on the isothermal transformation kinetics curve of steel, also known as the Time-Temperature-Transformation (TTT) curves:

$$n=\frac{\ln\left[\frac{\ln(1-f_1)}{\ln(1-f_2)}\right]}{\ln(t_1-t_{s,1})-\ln(t_2-t_{s,2})} \tag{15}$$

$$b=-\frac{\ln[1-f_1]}{(t_1-t_{s,1})^n} \tag{16}$$

where t_1 and t_2 are the isothermal times corresponding to the transformed fraction of f_1 and f_2 respectively in the TTT curves. $t_{s,1}$ and $t_{s,2}$ are the incubation periods corresponding to the transformed fraction of f_1 and f_2, respectively. The values of f_1 and f_2 are typically set to 1% and 99%, respectively.

The JMAK equation is applicable to the isothermal transformation process. For a continuous cooling process, it can be considered as a sequence of small isothermal steps. The incubation rate is accumulated using Scheil's additivity rule [25]. Therefore, the occurrence of phase transformation can be determined by satisfying the following equation:

$$\sum_{i=1}^{inc}\frac{\Delta t_i}{t_{s,i}}=1 \tag{17}$$

where *inc* is the current increment step, Δt_i is the time for the ith incremental step, $t_{s,i}$ is the isothermal incubation period at the temperature of the ith incremental step. The transformed fraction of ith step can be calculated as follows:

$$f_i=1-\exp\left(-b_i\left(t_i^*+\Delta t_i-t_{s,i}\right)^{n_i}\right) \tag{18}$$

$$t_i^*=\left[\frac{-ln(1-f_{i-1})}{b_i}\right]^{1/n_i}+t_{s,i} \tag{19}$$

where f_i and f_{i-1} are the transformed fraction of ith and $i-1$ th step.

In martensitic transformation, the transformed volume fraction of martensite is a function of undercooling. Koistinen and Marburger [26] proposed a relationship between the martensite fraction and temperature:

$$f = 1 - \exp(-a(M_s - \mathrm{T})) \tag{20}$$

where M_s is the start temperature of martensitic transformation, a is the constant reflecting the transformation rate and varying with the steel composition.

For 42CrMo steel, the JMAK model combined with Scheil's additivity rule provides a practical description of diffusional phase transformations under continuous cooling conditions, since the kinetic parameters are derived from its TTT data [27]. Although rapid cooling may introduce local non-equilibrium effects, the additivity rule enables the continuous cooling process to be reasonably approximated as a sequence of incremental isothermal steps. For martensitic transformation, the Koistinen–Marburger relation captures the dominant dependence of martensite fraction on undercooling and is therefore suitable for engineering simulations of alloy steels.

2.4. Online Simulation Process

The proposed mathematical model is applied to the online simulation of the end-quenching process of 42CrMo steel. The procedure for online simulation is shown in Figure 1 and can be outlined as follows:

1. Initialization stage: The purpose of this stage is to acquire the POD orthogonal basis. To achieve this objective, a finite element model (FEM) was initially established. Subsequently, the FOM of the transient temperature field was employed to compute nodal temperatures at various time steps. The snapshot matrix was constructed utilizing the nodal temperature values derived from the FOM. The snapshot matrix underwent SVD, and the first s terms of the left singular vector were truncated, resulting in the acquisition of the POD orthogonal basis. The value of s should be chosen to ensure that the energy proportion of the POD mode $\boldsymbol{I}_s$ surpasses 0.99. To assess the adequacy of this selection, we conducted a sensitivity analysis by varying s and examining the corresponding cumulative energy fractions and their impact on the resulting prediction errors. This analysis provides guidance for selecting an appropriate ROM order in transient simulations.
2. Loop iteration stage: The purpose of this stage is to address the computation of temperature and microstructure fraction under varying heat transfer boundary conditions during online simulation. As the heat transfer conditions alter throughout the quenching process, the matrices $\boldsymbol{K}$, $\boldsymbol{M}$ and $\boldsymbol{F}$ are updated at the beginning of each time step in accordance with the actual quenching process. Subsequently, the coefficient column vector $\boldsymbol{\alpha}$ is determined through the ROM of the transient temperature field. Consequently, the nodal values are reconstructed according to Equation (11). The volume fraction of the microstructure is determined based on the nodal temperatures. The aforementioned steps are iterated in each simulation increment until the final time is reached.

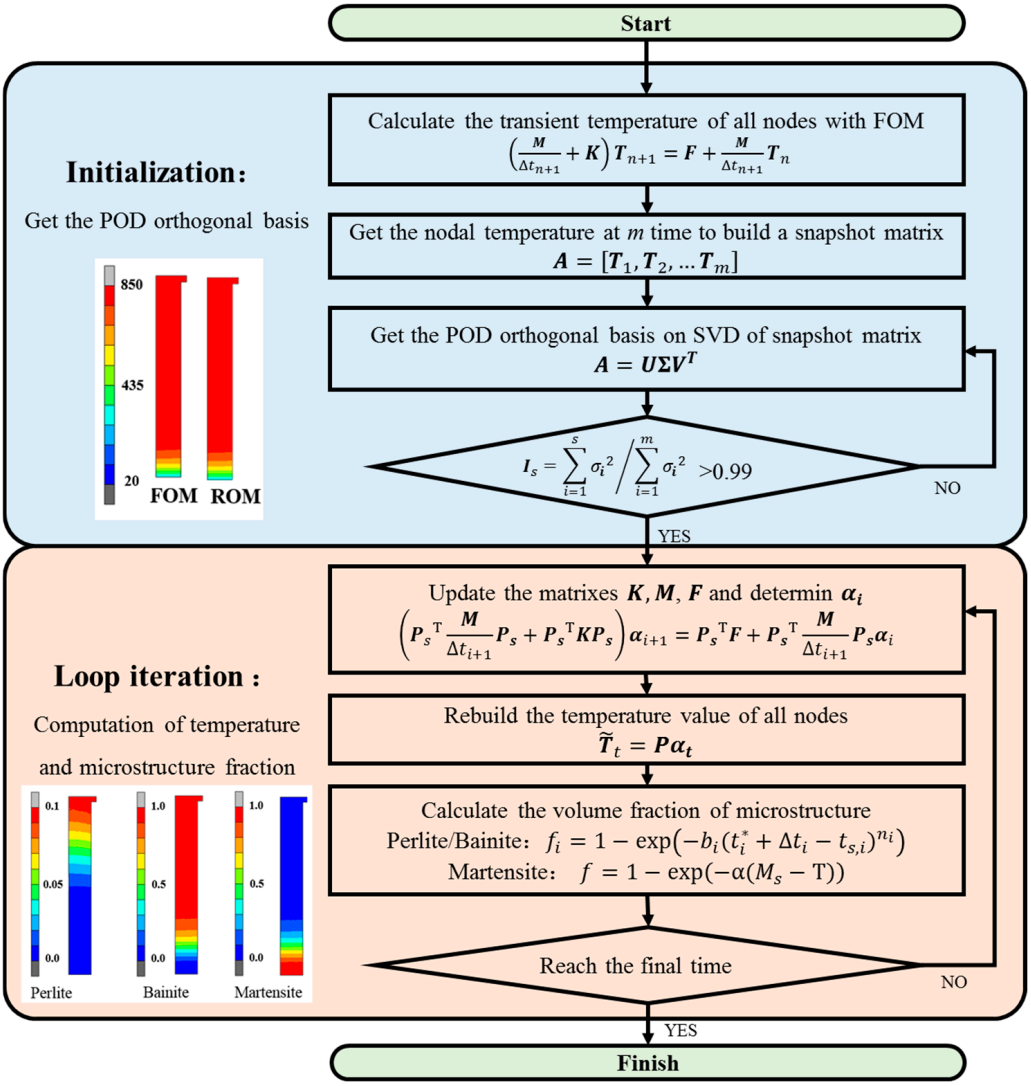


Figure 1. Flow of online simulation model of the end-quenching process.

3. Online Simulation of End-Quenching Process

3.1. FE Model

Figure 2 is the illustration of the end-quenching process. The material of the cylindrical sample is 42CrMo steel, which is assumed to be isotropic, and its thermal properties—thermal conductivity and specific heat—are temperature-dependent and exhibit nonlinear behavior, as referenced in our previous work [28]. The cylindrical sample was heated to 850 °C for 30 min. Following removal from the furnace, the sample was promptly transferred to an end-quenching test station, where water was sprayed until it cooled to room temperature. Online simulation and experiment of continuous water end-quenching (CWEQ) and water–air alternation end-quenching (WAEQ) are conducted. The WAEQ process is achieved by controlling the cessation and resumption of water spray cooling.

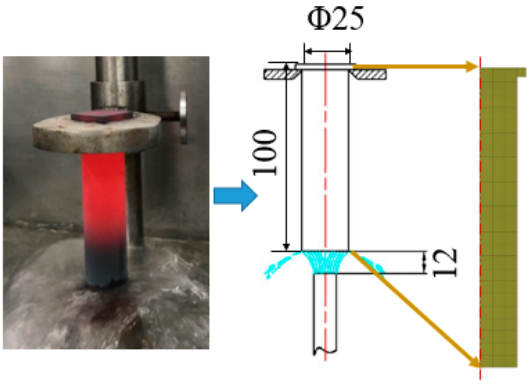


Figure 2. Illustration and simulation model of the end-quenching process (unit: mm).

Due to the axisymmetric nature of the end-quenching cylindrical sample, a two-dimensional axisymmetric model was employed for modeling. To ensure the numerical accuracy of the full-order model, convergence analyses in both space and time were performed. The mesh size and time increment were successively refined, and the corresponding temperature evolution was examined. When the element size was refined to 0.5 mm and the time increment was reduced to 0.1 s, further refinement resulted in negligible changes in the simulated temperature field. Therefore, a mesh with an element size of 0.5 mm was adopted, resulting in 5036 elements and 5268 nodes, and a time step of 0.1 s was selected for the simulations. The initial node temperature was set to 850 °C. The bottom boundary was assigned a heat transfer coefficient of water cooling, while the remaining boundaries were set to air convection [29]. The total cooling time was set to 1000 s to ensure complete cooling of the specimen to room temperature. The ROM of the temperature microstructure-coupled field was developed using the C++ language. The FOM calculation was performed using the commercial finite element software MSC.Marc 2018.

3.2. FOM Simulation Results of CWEQ

Figure 3 illustrates the temperature distributions at different times during the CWEQ process. It can be observed that the temperature is lowest at the end of the sample and highest at the top during the quenching process. However, since contact heat transfer with the support was not considered, the top temperature slightly deviates from the actual situation. Nevertheless, this deviation does not significantly affect the overall temperature simulation results. The temperature is relatively consistent in the radial direction, indicating that the air cooling on the side walls has a minimal impact on the temperature field. The cooling of the sample is primarily achieved through contact with the spray water on the end.

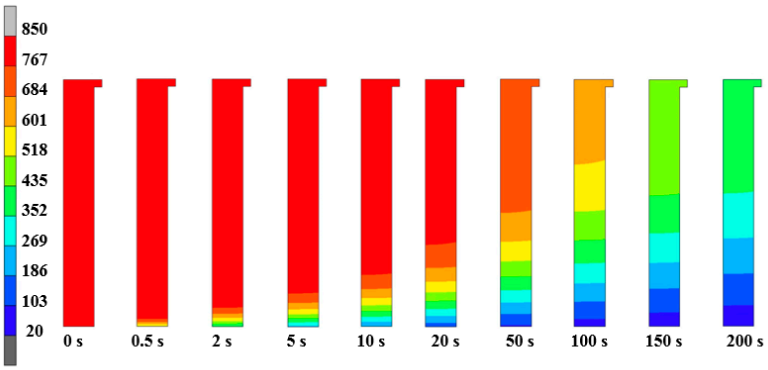


Figure 3. Temperature distributions at different time during the CWEQ process.

3.3. ROM Simulation Results of CWEQ

Based on the FOM simulation results of the CWEQ process, a snapshot matrix is constructed by collecting temperature data of all nodes at intervals of 1 s within the time range of 0 to 1000 s. The dimension of the snapshot matrix is 5268 × 1001, capturing temperature variation characteristics from 850 °C to room temperature. By employing the method described in Section 2, ROM with various reduced orders can be obtained.

Figure 4 presents a comparison between the simulated temperature distributions at different times (5 s, 50 s and 200 s) using FOM and ROM with different reduced orders (1, 3, 7, and 10). It is evident that there is a substantial difference in temperature distribution between the FOM result and the ROM result, with the order of 1 and 3. However, the temperature distribution trend of the ROM is similar to the FOM, depicting lower temperature at the end and higher temperature at the top. When the reduced order reaches 7, the temperature distribution pattern of the ROM closely aligns with that of the FOM. Further increasing the reduced order to 10 makes it difficult to visually discern differences in the results from the cloud plot.

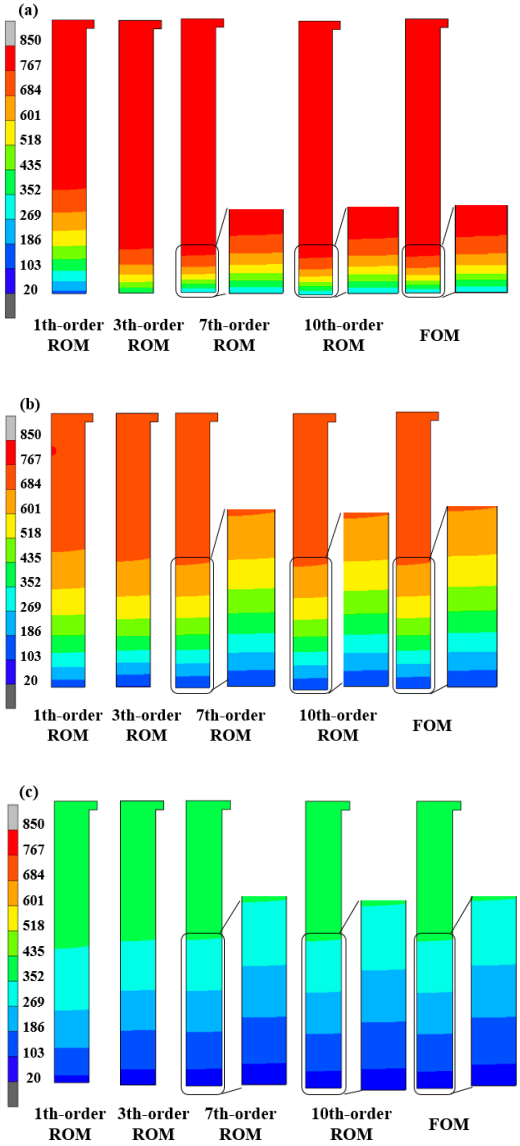
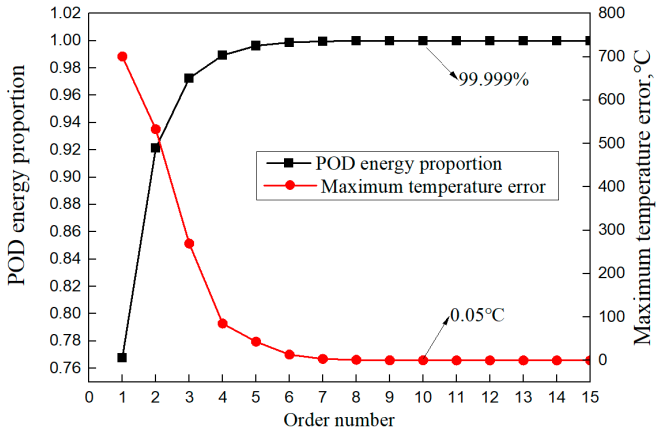
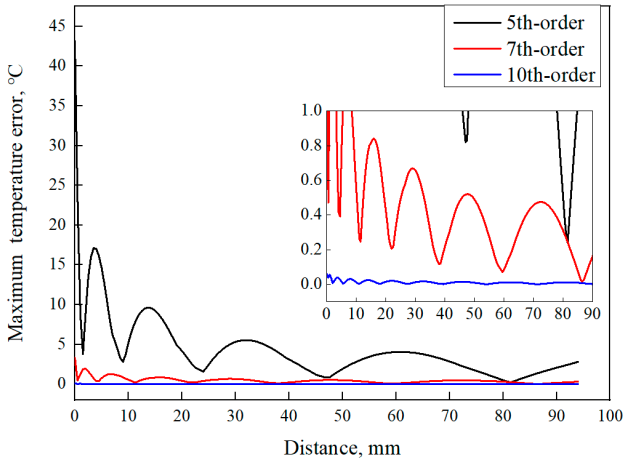


Figure 4. Simulated temperature distribution at (**a**) 5 s, (**b**) 50 s, (**c**) 200 s by using FOM and ROM with different reduced orders.

The energy proportion of the POD mode I_s of ROM with different orders was used to evaluate the information accuracy of ROM, as depicted in Figure 5a. At the 1st order, the value of I_s is 76.8%. As the order increases, I_s quickly rises, reaching a remarkable 99.999% at the 10th order. Additionally, the maximum nodal temperature error between ROM and FOM was analyzed. At the 1st order, the maximum nodal temperature error was 850 °C, while at the 10th order, the maximum nodal temperature error was 0.05 °C. Therefore, the 10th-order ROM was used for the subsequent analysis. Figure 5b shows the maximum temperature error versus distance from the quenched end for different ROM orders. The temperature error exhibits spatial oscillations because truncating higher-order POD modes removes fine-scale spatial variations, causing alternating over and under estimations at different nodes. The maximum error occurs at the quenched end at the start of cooling, where the temperature gradient is steepest. As the number of retained modes increases, both the overall error and the amplitude of the oscillations decrease.



(**a**)



(**b**)

Figure 5. (**a**) Energy proportion and maximum error curves of ROM with different orders. (**b**) Maximum temperature error versus distance from the quenched end for different ROM orders.

Figure 6 illustrates the simulated distribution curves of ferrite, bainite, and martensite volume fractions after the CWEQ process. Additionally, the distribution of Rockwell hardness has been determined experimentally. The result indicates that a complete martensitic microstructure is obtained within a depth of 7 mm from the surface. In the range of 7–30 mm depth, a mixture of martensite and bainite is present, while the remaining regions primarily consist of bainite. On the upper surface, the volume fraction of pearlite is less

than 10%. The hardness of 42CrMo steel is mainly determined by martensite content. The experimental measured hardness distribution fits well with the simulated martensite fraction distribution, thus confirming the accuracy of the simulation. Figure 7 shows the SEM images of the microstructure at 0/10/20/30 mm from the end surface. The microstructure is lath martensite at the spray end. The fraction of granular bainite increases with the increasing of distance.

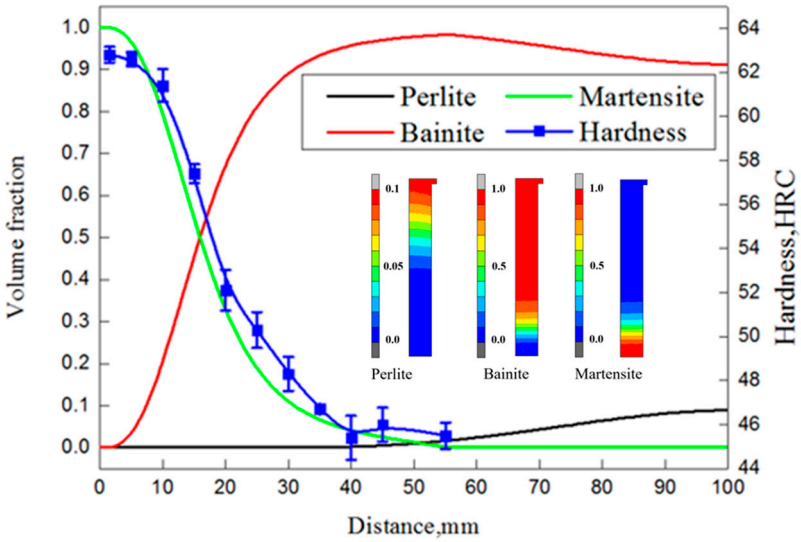


Figure 6. Simulated microstructure volume fraction and experimental measured hardness distribution curves after the CWEQ process.

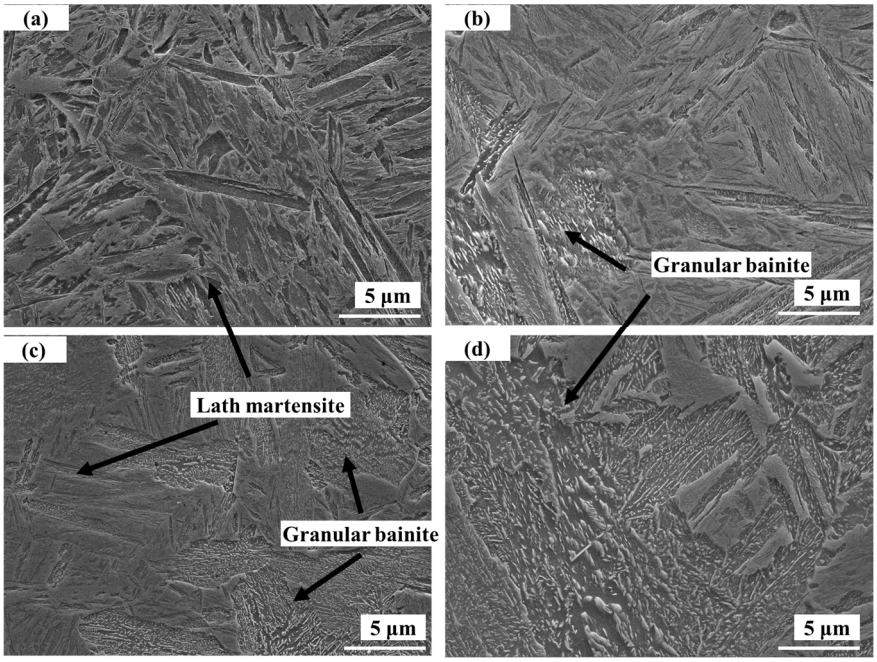


Figure 7. SEM images of microstructure at (**a**) 0 mm, (**b**) 10 mm, (**c**) 20 mm, (**d**) 30 mm from the end surface after the CWEQ process.

Table 1 shows the comparison of FOM and ROM simulation. When employing the 10th-order ROM for computation, the efficiency of solving is significantly enhanced. This is due to the reduced scale of solving the linear equation system, which now comprises 10 equations for each increment. In this study, a workstation with a CPU of Intel Core i9-7900 X CPU @ 3.30 GHz and 127 GB RAM is used. In terms of simulation time, FOM requires

7038 s to complete the simulation, whereas ROM takes 7.5 s. A substantial computation time reducing, by a factor of 938, is achieved for this particular problem. The primary reason is the reduction in the model's degrees of freedom from 5268 to 10 through the adoption of the ROM model. Additionally, the first ten basis functions capture almost 100% of the transient heat transfer process. This approach ensures the preservation of key characteristics in matrix operations.

Table 1. Comparison of FOM and ROM simulations of CWEQ.

Model	Number of Steps	Maximum Error/°C	Time Consuming/s	Storage/MByte
FOM	10,000	-	7038	748
ROM	10,000	0.05	7.5	1.16

Moreover, FOM necessitates storing all node data for every step, leading to a matrix size of 5248 × 10,001. This means the storage requirement for all time steps is 748 Mbyte. In contrast, ROM requires storing the coefficient column vector matrix of the POD orthogonal basis, which has a size of 10 × 10,001 and occupies 1.16 Mbyte. When there is a need to extract the node temperature values at a specific time, the data reconstruction can be performed using Equation (11), resulting in the nodal temperature corresponding to that specific time.

3.4. FOM and ROM Simulation Results of WAEQ

In the aforementioned analysis, ROM was obtained through the simulation of the CWEQ process. In order to assess the applicability of the obtained ROM for time-varying heat boundary conditions, the proposed 10th-order ROM is employed to simulate the WAEQ process in this section.

Figure 8 illustrates the simulated temperature curves using FOM and ROM at different positions during the WAEQ process, with a total of seven random water–air alternation cycles. The results indicate a close agreement between FOM and ROM simulation. Figure 9 depicts the maximum temperature error between FOM and ROM at various times. It can be observed that the error fluctuation is consistent with the frequency of water-air alternation. This phenomenon mainly arises from the fact that when temperature gradients are steep, the snapshot matrix struggles to accurately reflect the temperature distribution characteristics of the model. However, the maximum temperature difference is 6.4 °C, achieving an accuracy of 99.2%. This level of precision is considered sufficient for simulating the temperature field in heat treatment processes, ensuring an adequate description of the overall temperature distribution. It is demonstrated that the applicability of the ROM developed by the CWEQ process to complex heat transfer boundary conditions.

Table 2 presents the maximum error, computation time, and required storage space during ROM and FOM simulation processes. It is evident that under complex heat transfer boundary conditions, the computation time using the ROM decreased by 1062 times (from 3612 s to 3.4 s). The storage space has been reduced by a factor of 619 (from 378 Mbyte to 0.62 Mbyte). The POD-ROM method has been widely recognized as an effective approach for reducing computational cost in transient temperature field simulations. In this study, we further demonstrate its reliability and efficiency for high-fidelity online simulation of the heat treatment process considered here.

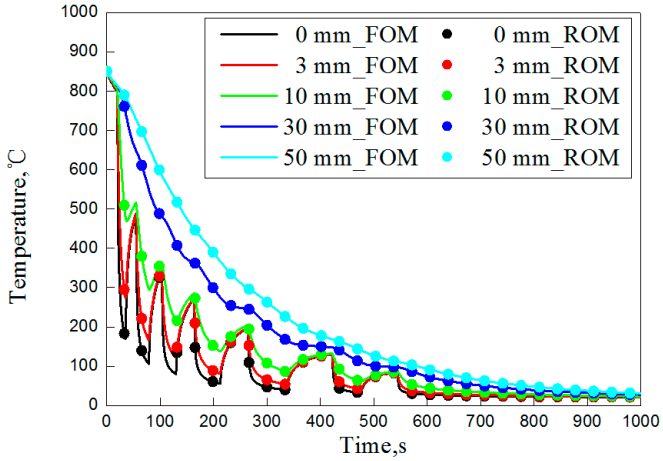


Figure 8. Simulated temperature curves using FOM and ROM at different positions during the WAEQ process.

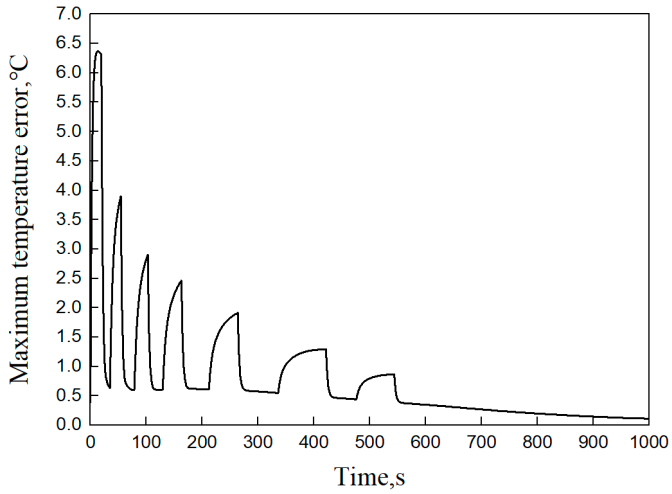


Figure 9. Maximum temperature error curves between FOM and ROM simulation of WAEQ process.

Table 2. Comparison of FOM and ROM simulation of WAEQ.

Model	Number of Steps	Maximum Error/°C	Time Consuming/s	Storage/Mbyte
FOM	5000	-	3612	378
ROM	5000	6.4	3.4	0.62

3.5. Online Simulation Platform for Digital Twin

Figure 10 illustrates the digital twin architecture for the heat treatment process. In the provided framework, the interaction between heat treatment equipment/process parameters in the physical space and the digital space is facilitated through sensor and control modules. This interaction establishes a bridge between the physical and digital spaces, creating a dynamic mapping within the digital space that accurately reflects the characteristics of the physical space. This digital twin framework offers the capability to visualize the real-time status of equipment and the distribution of physical fields within heat-treated components. Furthermore, it enables the analysis and control of equipment and processes based on the digital twin data.

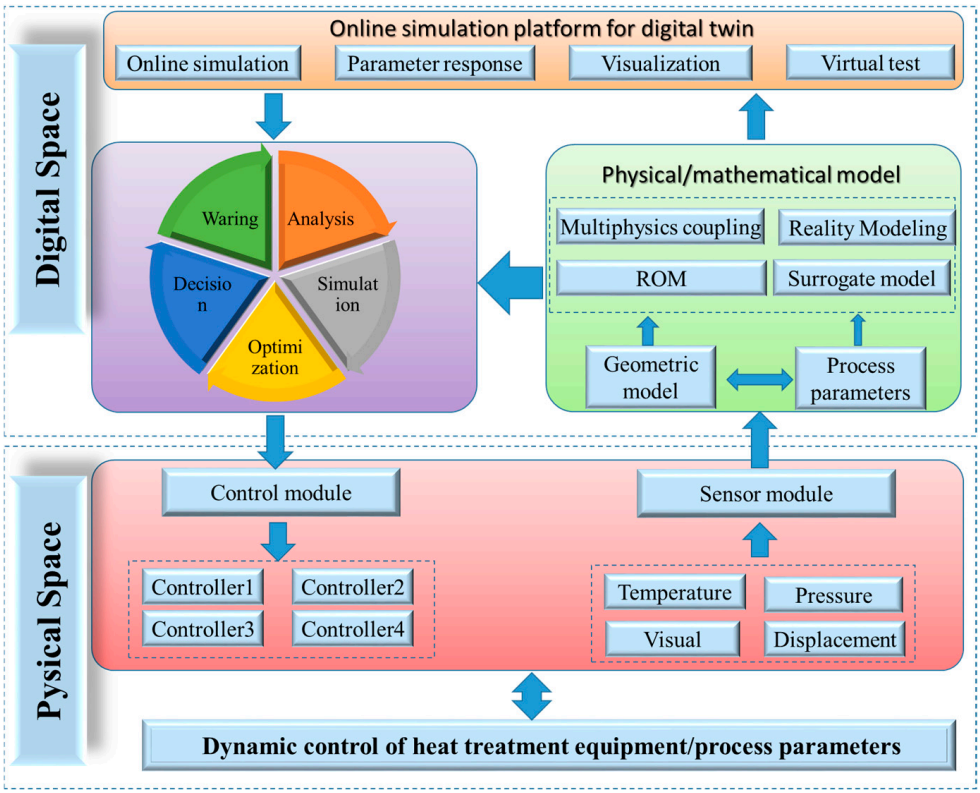


Figure 10. Digital twin architecture for the heat treatment process.

Within this architecture, the online simulation platform for heat treatment digital twin is a visualization system that integrates physical and mathematical models. It enables the online simulation of the physical space, parameter response, visualization of physical field and data, as well as virtual tests. The platform also serves as a foundation for intelligent analysis, simulation, optimization, decision-making, and early warning throughout the heat treatment process.

In this study, an online simulation platform for the end-quenching process was developed based on the proposed ROM, as shown in Figure 11. This platform enables real-time online simulation of CWEQ and WAEQ processes. The spray-/water-quenching status of the platform corresponds to the physical world. Furthermore, the temperature at a point located 20 mm from the end is measured using an infrared thermometer. This measured temperature is then transmitted in real time to the online simulation platform, represented as "Tested" in the temperature curve chart on the upper-right side of the platform. The "Simulation" corresponds to the real-time simulated data for the same location. The chart in the lower-right section of the platform represents the volume fraction of the microstructure at that specific location. In the center, the platform provides the real-time temperature distribution on the end-quenched sample, which can be toggled to show the volume fraction distribution of austenite, pearlite, bainite, and martensite. The upper-right corner displays the current spray/air quenching status and current time.

The online simulation platform primarily accomplishes real-time dynamic calculation and visualization of the temperature and microstructure fields during the end-quenching process. We also conducted an assessment of the platform's real-time capabilities. The results indicate that the computational time required for each update of the online simulation platform is 0.4 s. Specifically, the computation time for the temperature field using ROM is approximately in the range of 10^{-5} to 10^{-4} s; the microstructure field calculation takes about 0.2 s; the model rendering and display consume another 0.2 s. It should be noted that the 0.4 s update interval reflects the time required for complete visualization and mi-

crostructure computation, not the temperature calculation itself. Since the temperature field computation is extremely fast, it is sufficient to meet the requirements of typical industrial temperature sampling frequencies (~50 Hz), even though control system commands are executed at microsecond intervals. Therefore, the platform is capable of supporting real-time monitoring and visualization of the heat treatment process. The simulated temperature data closely aligns with the measured data. This platform addresses challenges related to the invisibility and immeasurability of component states during the end-quenching process. It provides a dynamic control foundation for complex heat treatment processes.

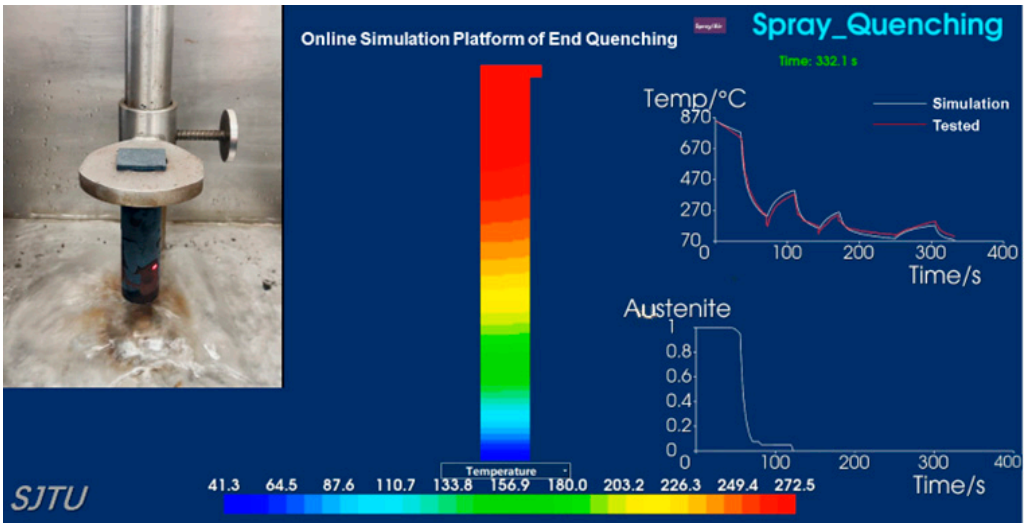


Figure 11. Online simulation platform of end-quenching process.

4. Conclusions

1. In this paper, the ROM of the transient temperature field calculation was constructed based on the POD method. This significantly reduces the size of the partial differential linear equation system to be solved during transient calculations. A coupled online calculation method for the temperature field and microstructure field during the heat treatment process was developed.
2. The ROM for the end-quenching process of 42CrMo steel was established, enabling simulations of both CWEQ and WAEQ scenarios. Compared with the FOM calculation by MSC.Marc, the computation time was significantly reduced 1062-fold by employing a 10th-order ROM, accompanied by a 610-fold reduction in storage space. The maximum relative deviation between FOM and ROM is 0.8%, which demonstrates the ROM's capability to meet the online simulation requirements for digital twinning.
3. A framework for the thermal treatment digital twinning system was proposed, and an online simulation platform for end-quenching was developed. This platform enables real-time prediction of temperature and microstructure evolution during the end-quenching process. The computation time for each step is 0.4 s. This research presents a novel approach for real-time control and rapid computation in the heat treatment process.

In future work, the proposed ROM-based online simulation framework will be extended and validated for components with more complex geometries. Furthermore, it will be utilized to investigate advanced cooling control strategies, such as alternating water and air quenching, with the aim of optimizing heat treatment processes.

Author Contributions: Conceptualization, M.G.; Methodology, M.G. and X.Y.; Software, M.G. and X.Y.; Validation, C.L. and J.G.; Formal analysis, M.G.; Investigation, M.G. and C.L.; Resources, C.L.; Data curation, M.G.; Writing—original draft, M.G.; Writing—review & editing, D.T. and J.G.; Supervision, D.T. and J.G.; Project administration, D.T. All authors have read and agreed to the published version of the manuscript.

Funding: This research received no external funding.

Data Availability Statement: The data presented in this study are available on request from the corresponding author due to privacy.

Conflicts of Interest: The authors declare no conflict of interest.

References

1. Yang, X.; Liu, X.; Zhang, H.; Fu, L.; Yu, Y. Meta-model-based shop-floor digital twin architecture, modeling and application. *Robot. Comput. Integr. Manuf.* **2023**, *84*, 102595. [CrossRef]
2. Soori, M.; Arezoo, B.; Dastres, R. Digital twin for smart manufacturing, A review. *Sustain. Manuf. Serv. Econ.* **2023**, *2*, 100017. [CrossRef]
3. Lalancette, F.; Désilets, M.; Pansiot, B.; LeBreux, M.; Bilodeau, J.-F. Dimensional reduction of a 3D thermoelectric model to create a reliable and time-efficient 2D model representing an aluminum electrolysis cell. *Int. J. Heat Mass Transf.* **2023**, *202*, 123777. [CrossRef]
4. Song, H.; Song, M.; Liu, X. Online autonomous calibration of digital twins using machine learning with application to nuclear power plants. *Appl. Energy* **2022**, *326*, 119995. [CrossRef]
5. Esfahani, A.K.; Babaei, M.; Sarrami-Foroushani, S. A numerical model coupling phase transformation to predict microstructure evolution and residual stress during quenching of 1045 steel. *Math. Comput. Simul.* **2021**, *179*, 1–22. [CrossRef]
6. Yu, B.; Tong, Y.; Hu, P.; Gao, Q. A novel inversion approach for identifying the shape of cavity by combining Gappy POD with direct inversion scheme. *Int. J. Heat Mass Transf.* **2020**, *150*, 119365. [CrossRef]
7. He, S.; Wang, M.; Zhang, J.; Tian, W.; Qiu, S.; Su, G.H. A deep-learning reduced-order model for thermal hydraulic characteristics rapid estimation of steam generators. *Int. J. Heat Mass Transf.* **2022**, *198*, 123424. [CrossRef]
8. Feeny, B.F.; Kappagantu, R. On the physical interpretation of proper orthogonal modes in vibrations. *J. Sound Vib.* **1998**, *211*, 607–616. [CrossRef]
9. Jiang, W.; Pan, T.; Jiang, G.; Sun, Z.; Liu, H.; Zhou, Z.; Ruan, B.; Yang, K.; Gao, X. Data-driven physical fields reconstruction of supercritical-pressure flow in regenerative cooling channel using POD-AE reduced-order model. *Int. J. Heat Mass Transf.* **2023**, *217*, 124699. [CrossRef]
10. Selimefendigil, F.; Öztop, H.F. Analysis of hybrid nanofluid and surface corrugation in the laminar convective flow through an encapsulated PCM filled vertical cylinder and POD-based modeling. *Int. J. Heat Mass Transf.* **2021**, *178*, 121623. [CrossRef]
11. Tanaka, H.; Nagai, H. Thermal surrogate model for spacecraft systems using physics-informed machine learning with POD data reduction. *Int. J. Heat Mass Transf.* **2023**, *213*, 124336. [CrossRef]
12. Hossain, M.N.; Bharti, C.; Ghosh, D. Energy preservation in POD based reduced order models for linearly vibrating systems. *Mech. Res. Commun.* **2023**, *128*, 104056. [CrossRef]
13. Jiang, G.; Kang, M.; Cai, Z.; Wang, H.; Liu, Y.; Wang, W. Online reconstruction of 3D temperature field fused with POD-based reduced order approach and sparse sensor data. *Int. J. Therm. Sci.* **2022**, *175*, 107489. [CrossRef]
14. Ansari, A.B. Reduced-order modeling of PEM fuel cell based on POD and PODI: An efficient approach toward combining highest accuracy with real-time performance. *Int. J. Hydrogen Energy* **2023**, *48*, 29327–29349. [CrossRef]
15. Chen, X.; Zhong, W.; Li, T. Fast prediction of temperature and chemical species distributions in pulverized coal boiler using POD reduced-order modeling for CFD. *Energy* **2023**, *276*, 127663. [CrossRef]
16. Aversano, G.; D'Alessio, G.; Coussement, A.; Contino, F.; Parente, A. Combination of polynomial chaos and Kriging for reduced-order model of reacting flow applications. *Results Eng.* **2021**, *10*, 100223. [CrossRef]
17. Mukhtar, A.; Yasir, A.S.H.M.; Nasir, M.F.M. A machine learning-based comparative analysis of surrogate models for design optimisation in computational fluid dynamics. *Heliyon* **2023**, *9*, e18674. [CrossRef]
18. Wang, L.; Dong, X.; Jing, L.; Li, T.; Zhao, H.; Zhang, B. Research on digital twin modeling method of transformer temperature field based on POD. *Energy Rep.* **2023**, *9*, 299–307. [CrossRef]
19. Li, T.; Gao, Y.; Han, D.; Yang, F.; Yu, B. A novel POD reduced-order model based on EDFM for steady-state and transient heat transfer in fractured geothermal reservoir. *Int. J. Heat Mass Transf.* **2020**, *146*, 118783. [CrossRef]
20. Zhu, Q.H.; Liang, Y.; Gao, X.W. A proper orthogonal decomposition analysis method for transient nonlinear heat conduction problems. Part 1: Basic algorithm. *Numer. Heat Transf. Part B Fundam.* **2020**, *77*, 87–115. [CrossRef]

21. Wang, Y.; Yu, B.; Cao, Z.; Zou, W.; Yu, G. A comparative study of POD interpolation and POD projection methods for fast and accurate prediction of heat transfer problems. *Int. J. Heat Mass Transf.* **2012**, *55*, 4827–4836. [CrossRef]
22. Chen, N.L.; Zhang, W.M.; Gu, J.F.; Zuo, X.W.; Xu, J. Development and application of alternate timed quenching by water and air. *Int. Heat Treat. Surf. Eng.* **2008**, *2*, 109–115. [CrossRef]
23. Gur, C.H.; Pan, J. *Handbook of Thermal Process Modeling Steels*; CRC Press: Boca Raton, FL, USA, 2008.
24. Sirovich, L. Turbulence and the dynamics of coherent structures. I. Coherent structures. *Q. Appl. Math.* **1987**, *45*, 561–571. [CrossRef]
25. Fernandes, F.M.B.; Denis, S.; Simon, A. Mathematical model coupling phase transformation and temperature evolution during quenching of steels. *Mater. Sci. Technol.* **1985**, *1*, 838–844. [CrossRef]
26. Koistinen, D.P.; Marburger, R.E. A general equation prescribing the extent of the austenite-martensite transformation in pure iron-carbon alloys and plain carbon steels. *Acta Metall.* **1959**, *7*, 59–60. [CrossRef]
27. Zhong, H.; Wang, Z.; Gan, J.; Wang, X.; Yang, Y.; He, J.; Wei, T.; Qin, X. Numerical simulation of martensitic transformation plasticity of 42CrMo steel based on spot continual induction hardening model. *Surf. Coat. Technol.* **2020**, *385*, 125428. [CrossRef]
28. Tong, D.; Gu, J.; Yang, F. Numerical simulation on induction heat treatment process of a shaft part: Involving induction hardening and tempering. *J. Mater. Process. Technol.* **2018**, *262*, 277–289. [CrossRef]
29. Tong, D.; Gu, J.; Totten, G.E. Numerical simulation of induction hardening of a cylindrical part based on multi-physics coupling. *Model. Simul. Mater. Sci. Eng.* **2017**, *25*, 035009. [CrossRef]

Disclaimer/Publisher's Note: The statements, opinions and data contained in all publications are solely those of the individual author(s) and contributor(s) and not of MDPI and/or the editor(s). MDPI and/or the editor(s) disclaim responsibility for any injury to people or property resulting from any ideas, methods, instructions or products referred to in the content.